

Phosphate-Mineralization Microbe Repairs Heavy Metal Ions That Formed Nanomaterials in Soil and Water

Xiaoniu Yu and Qiwei Zhan

Abstract

This chapter presents a new method for treatment of heavy metal ions in soil or water. Heavy metal pollution in soil and water has become one of the serious environmental problems. Heavy metal pollution can degrade soil quality and ecosystems, contaminate crops, and threaten human health. At present, there are three ways to repair heavy metals in soil or water, including physical, chemical, and biological technologies. The microbial mineralization technology can be applied to remove heavy metal pollutants which contaminated soil and water and has been paid with more attention in recent years. Heavy metal ions can be mineralized by phosphate-mineralization microbe to form stable phosphate nanomaterials compared to mineralization of carbonate-mineralization microbe in the environments. Therefore, heavy metal pollution can well be removed from soil or water by microbial mineralization method.

Keywords: heavy metal pollution, soil, water, phosphate-mineralization microbe, phosphate nanomaterials

1. Introduction

The density of the heavy metal is bigger than 4.5 g/cm^3 or more, and atomic numbers are from 23 (V) to 92 (U) of heavy metal elements, such as lead, nickel, zinc, copper, iron, cadmium, chromium, etc. [1]. They are widely used in industrial production and discharged into the environment due to the failure to process heavy metals in mining and industrial production. Soil and water are the ultimate destination of these heavy metals due to their particularity. Compared with air pollution, water pollution, and industrial solid waste pollution, heavy metals in soil and water are invisible and concealed. The pollution of heavy metals in soil and water can lead to the degradation of soil fertility, the reduction of crop yields, and the decline in quality, which seriously affects the environmental quality and sustainable economic development and threatens people's food safety [2]. Heavy metal pollution has become a global concern [1, 3–9]. Whether in the soil or water, different heavy metals enter the bottom of the human food chain and finally enter the human body [2]. Heavy metals are very difficult to be biodegraded and can easily be biomagnified in the human body. Heavy metals can interact strongly with proteins and enzymes in the human body, making them inactive, or they can accumulate in certain organs of the human body, causing chronic poisoning, which is a serious threat to people's lives, health, and safety [2, 5].

The content, migration, and damage of heavy metal ions are high in the electroplating wastewater irrigation area, the tailings accumulation area, and the surrounding cultivated soil. Since heavy metal pollution has already caused a major threat to human survival and health, countries around the world have formulated corresponding laws and regulations to strictly limit the emission of heavy metals. At the same time, areas of heavy metal pollution can well be repaired through physical, chemical, and biological technologies to reduce the harm [9]. Physical and chemical methods to repair heavy metal pollution have been widely reported, including chemical curing, soil leaching, electrokinetic repair, etc. The physicochemical methods may cause secondary pollution because of its damage to soil structure and indigenous microorganisms. Bioremediation technology is a more effective method for controlling polluted soil and water and has become a new hotspot in current environmental engineering science and technology research, including phytoremediation, microbial adsorption, and microbial mineralization technologies. The use of microorganisms (bacteria, algae, yeast, etc.) to reduce or eliminate heavy metal pollution has been reported widely at home and abroad. The mechanism of bioremediation heavy metals includes: (1) cell metabolism—a specific metabolic pathway can make heavy metal ions precipitation or into low-toxic; (2) biosorption—using living cells, inanimate organisms metal-binding proteins and polypeptides or biopolymers as biosorbents, vacuolar swallowing, precipitation and redox reactions; and (3) biomineralization—heavy metal ions are precipitated into biominerals by microbial hydrolysate.

At present, the problem of heavy metal pollution in soil and water is becoming more and more serious, and the use of carbonate-mineralization microbe to repair heavy metals pollution has attracted people's attention because of its excellent characteristics [10, 11]. Although many studies have been carried out, the stability of carbonate in the environment is lower than that of phosphate. Therefore, this chapter proposes that phosphate-mineralization microbe mineralizes heavy metal ions to form stable phosphates. Based on the principle of biomineralization, organic phosphate monoester is hydrolyzed by phosphatase produced by phosphate-mineralization microbe of growth and metabolism and then obtains phosphate ions. Heavy metal ions can combine with phosphate ions to form phosphate minerals in soil or water, thereby reducing the risk of heavy metals being absorbed by plants and the harm to the natural environment.

2. Methodology

Bacillus subtilis was purchased by China Center of Industrial Culture Collection. Pure water was made by small ultrapure water machine. All raw materials were of analytically pure grade and used without further purification.

Bacillus subtilis of cultivation [12, 13]: 5 g of tryptone and 3 g of beef extract were completely dissolved in 1 L of pure water, and its pH was adjusted to 7.0 using diluted NaOH solution. 1 L of above solution was added to two beaker flasks (1000 mL), and each bottle was added 500 mL of mixture solution and wrapped by paper and gauze. Two beaker flasks were placed in autoclave under 125°C and 0.1 Mpa for 30 min. Then they were cooled to room temperature under natural conditions. Next, 3 mL of *Bacillus subtilis* strains were added to each beaker flask and cultivated in the oscillation incubator ($170\text{r}\cdot\text{min}^{-1}$) at 28°C for 22–24 hours. As a result, the harvested microorganisms were kept in a refrigerator at 4°C before use. Optical density (OD) of *Bacillus subtilis* liquid was measured by UV spectrophotometer at 600 nm of wavelength with OD range of 1.23–1.36.

Syntheses of barium phosphates [14]: organic phosphate monoester (pH = 8.8–9.3) was added to 100 mL of *Bacillus subtilis* under static conditions for 24 hours at room temperature. The mixture solution of *Bacillus subtilis* and organic phosphate monoester was centrifuged, and then the centrifugal solution was obtained. The pH of solution was adjusted to 7, 8, 9, 10, and 11 with diluted HCl and NaOH solution. BaCl₂·2H₂O powder was added to the above solution at different pH. Precipitated solution was stilled for 24 hours at room temperature after stirring for 1 min. All products were dried at 60°C for 24 hours. After that, all powder precipitates were collected.

Microbiological reduction-precipitation of cerium phosphates [15]: Organic phosphate monoester (pH = 8.8–9.3) was added to 100 mL of *Bacillus subtilis* under static conditions for 24 hours. Next, 0.01 and 0.02 mol of Ce(SO₄)₂ were added to above solution. The precipitated solution was stood under static conditions for 24 hours. As a result, two powder precipitates were dried at 60°C for 24 hours. After that, two powder specimens were collected and characterized.

Syntheses of iron phosphates [16]: Organic phosphate monoester (pH = 8.8–9.3) was injected into 200 mL of *Bacillus subtilis* and was allowed to stand under static conditions for 24 hours at room temperature. After 24 hours, FeSO₄·7H₂O (12 mM) was added to the above mixture solution with 2 min of stirring. The precipitated solution was allowed to stand under static conditions for 72 hours at room temperature. The products were then dried at 60°C for 24 hours. After that, powder precipitates were obtained and characterized.

Fourier-transform infrared spectroscopy (FTIR) spectra of the samples were recorded with a Nicolet 5700 spectrometer using the KBr pellet technique in the range of 399–4000 cm⁻¹. The phase purity of products was examined by powder X-ray diffraction (XRD) with a Bruker D8-Discover diffractometer with Cu K α radiation ($\lambda = 1.5406 \text{ \AA}$). Scanning electron microscopy (SEM, FEI Company, the Netherlands, operating voltage 20 kV) with an energy-dispersive X-ray spectroscopy (EDS) was used to conduct morphological studies and to measure elemental compositions of the samples. Transmission electron microscopy (TEM) images were obtained on a FEI, G2 20 equipment. The samples were dispersed in anhydrous ethanol before being tested. Thermogravimetric-differential scanning calorimetry (DSC-TG) was carried out on STA449 F3 thermogravimetric analyzer (NETZSCH, Germany). The analyses were carried out simultaneously in a nitrogen atmosphere at a heating rate of 10°C/minute between room temperature and 700–800°C under an N₂ flow of 20 mL·min⁻¹. The average crystallite size of biophosphate nanomaterials was estimated by the Scherrer formula [13]:

$$D = \frac{k\lambda}{\beta \cos\theta} \quad (1)$$

where D is the average crystallite size of samples (nm), k is the shape factor (0.9), λ is the wavelength of Cu K α radiation equal to 1.5406 Å, β is defined as the full width of the peak at half of the maximum intensity (FWHM), and θ is the diffraction angle of the selected reflection.

3. Barium phosphate nanoparticles prepared by microbial mineralization method

The FTIR spectra of barium phosphates obtained at pH = 8 and 11 were displayed in **Figure 1**. The peak at 3415.62 cm⁻¹ was KBr mull absorption, which appears in the spectrum of any compounds. A shoulder peak at 2973.47 cm⁻¹

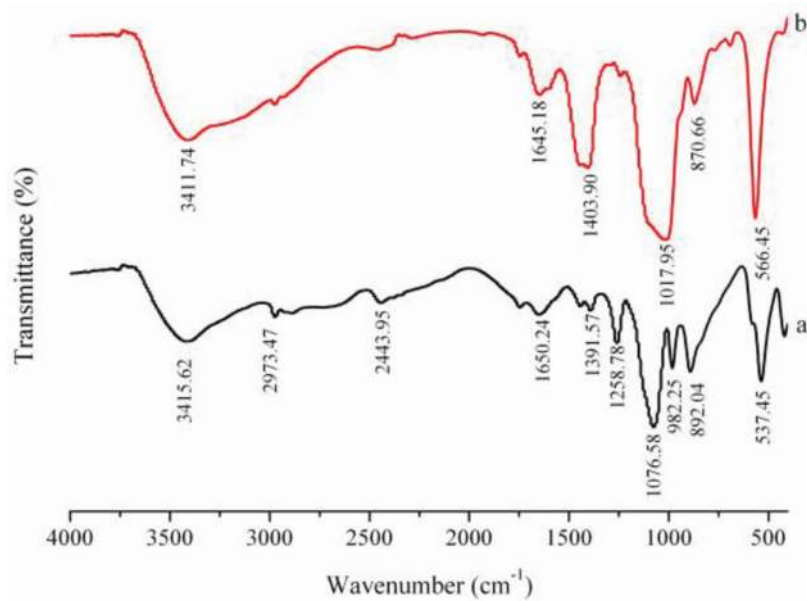


Figure 1. FTIR spectra of barium phosphates prepared at pH = 8 (a) and 11 (b) [14].

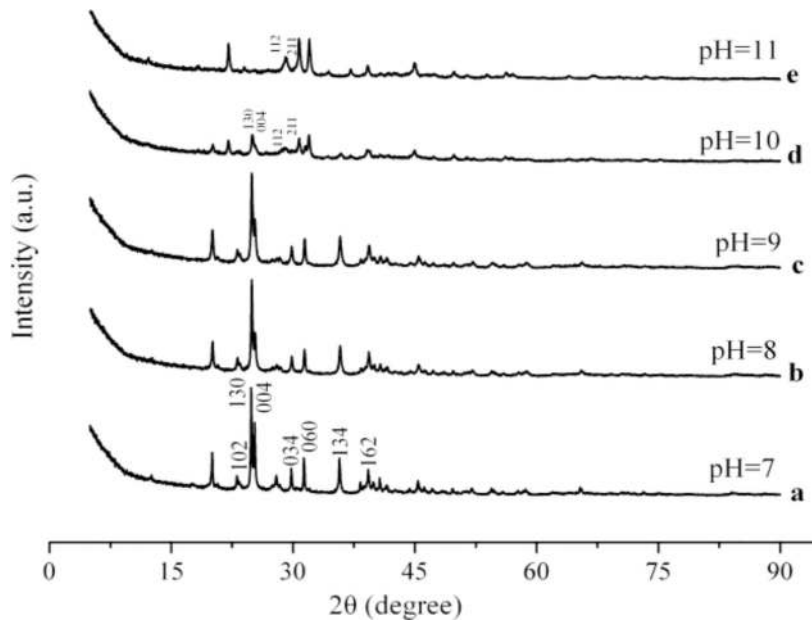


Figure 2. XRD patterns of barium phosphates precipitated at pH = 7, 8, 9, 10, and 11 [14].

corresponded to hinder rotation. The peak at 1650.24 cm^{-1} reveals thermal vibrations of H^+ in an intermolecular phonon vibration associated with $\text{H}^+\text{-PO}_4^{3-}$. The peak at 1258.78 cm^{-1} was P=O stretching vibration. The peaks at 1391.75 , 1076.58 , and 982.25 cm^{-1} corresponded to stretching vibration of P-O (H). The P=O of deformation vibration was found at 892.04 cm^{-1} and to be nondegenerate. The P-O(H) wagging and rocking vibration was found at 537.45 cm^{-1} . The above results are similar with literatures reported, as shown in **Figure 1a** [17–20]. The peaks are at 3411.74 , 1645.18 , 1403.90 , 1017.95 , 870.66 , and 566.45 cm^{-1} in the FTIR spectrum with respect to the OH and PO_4^{3-} (**Figure 1b**), which were in accordance with the data reported in the literature [21].

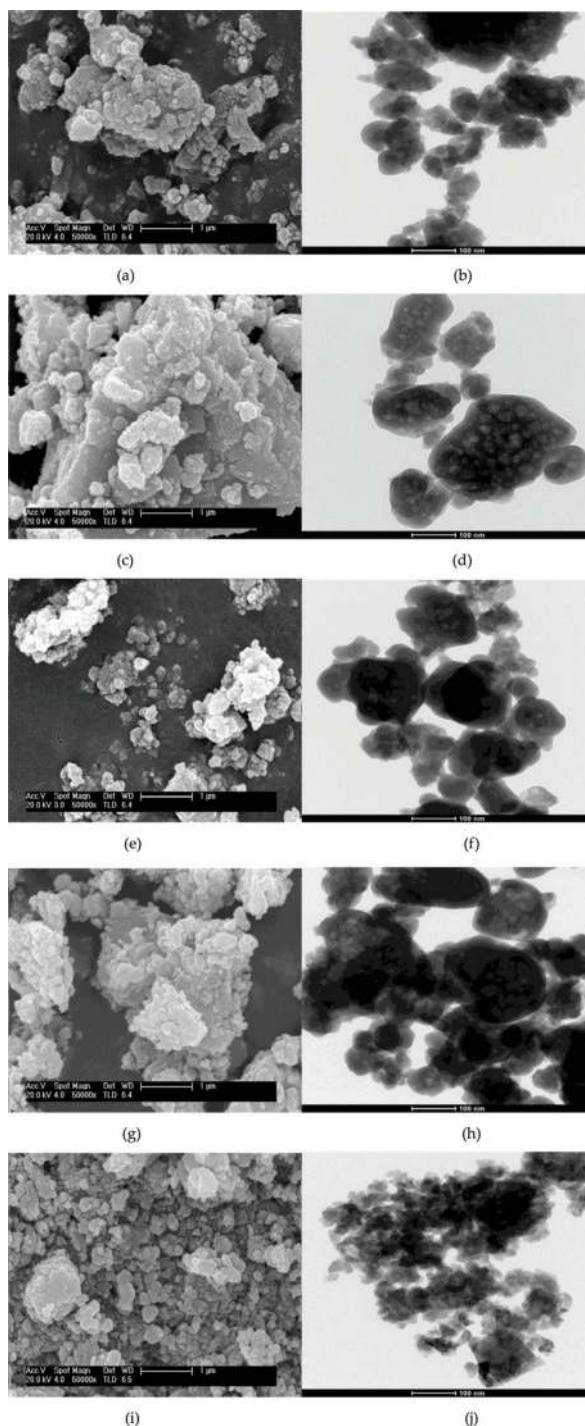


Figure 3. SEM and TEM images of barium phosphates: (a, b) pH = 7, (c, d) pH = 8, (e, f) pH = 9, (g, h) pH = 10, and (i, j) pH = 11 [14].

Chemical compositions of barium phosphates were analyzed by XRD technique, as shown in **Figure 2**. Barium phosphates of patterns could be readily indexed using the reported structures of BaHPO_4 (JCPDS Card No. 72-1370) at pH < 10 (**Figure 2a-c**). When pH was 10, the mixture of BaNaPO_4 , BaHPO_4 , and $\text{Ba}_5(\text{PO}_4)_3\text{OH}$ (JCPDS No. 70-1787, 09-0113 and 36-0272) was found, as shown in **Figure 2d**. The mixture of BaNaPO_4 (JCPDS No. 70-1787) and $\text{Ba}_5(\text{PO}_4)_3\text{OH}$ (JCPDS No. 78-1441) was precipitated at pH = 11 (**Figure 2e**). Above results

indicated that HPO_4^{2-} and PO_4^{3-} ions were obtained by *Bacillus subtilis* hydrolyzing organic phosphate monoester. HPO_4^{2-} ions were formed at pH = 7, 8, and 9. HPO_4^{2-} and PO_4^{3-} ions were formed at pH = 10. PO_4^{3-} ions were formed at pH = 11. Therefore, the barium phosphates were mainly BaHPO_4 at pH < 10 [22]. The barium phosphates were mainly the mixture of BaNaPO_4 , BaHPO_4 , and $\text{Ba}_5(\text{PO}_4)_3\text{OH}$ at pH = 10 [22]. The barium phosphates were mainly the mixture of BaNaPO_4 and $\text{Ba}_5(\text{PO}_4)_3\text{OH}$ at pH = 11 [22]. Organic phosphate monoesters can well be hydrolyzed through *Bacillus subtilis*.

SEM and TEM images showed shape of barium phosphates were nanoparticles, as shown in **Figure 3**. SEM images showed that barium phosphates were nano-agglomerates, (**Figure 3a, c, e, g, and i**). The size of the nano-agglomerates was less than 3 μm . TEM images indicated that morphology of barium phosphate particles was mainly irregular flakes with diameter in the range of 20–100 nm, as shown in **Figure 3b, d, f, h, and j**. The average size of barium phosphates was calculated by the Scherrer formula (1), and the average size was 48.56, 36.60, 31.89, 33.27, and 34.79 nm when pH were 7, 8, 9, 10, and 11, respectively [13]. Above results showed that barium phosphate nanomaterials could be easily prepared by the centrifuged solution of *Bacillus subtilis* and organic phosphate monoester reacting with $\text{BaCl}_2 \cdot 2\text{H}_2\text{O}$, which were different from chemical and biomineralization methods [17, 22].

4. Microbiological reduction-precipitation of nanostructured cerium phosphates

Elemental compositions of cerium phosphates were analyzed by EDS spectra, as shown in **Figure 4**. The elements C, O, Na, P, S, and Ce were found in cerium phosphates when P/Ce molar ratio was 1:1 and 2:1 (**Figure 4a and b**). The raw files and cerium phosphates could be indexed by MDI jade 5.0 procedure. The indexed results indicated $\text{CePO}_4 @ \text{NaCe}(\text{SO}_4)_2(\text{H}_2\text{O})$ and CePO_4 were found when P/Ce molar ratio was 1:1 and 2:1, respectively, as shown in **Figure 5a and b**. The standard cards of $\text{CePO}_4 @ \text{NaCe}(\text{SO}_4)_2(\text{H}_2\text{O})$ used were JCPDS Card No. 74–1889 and 86–0526. CePO_4 was JCPDS Card No. 75–1880.

The average crystallite size of cerium phosphates was calculated via the Scherrer formula (1), as shown in **Table 1** [13]. The results showed that the average size of $\text{CePO}_4 @ \text{NaCe}(\text{SO}_4)_2(\text{H}_2\text{O})$ nanoparticles was bigger than CePO_4 .

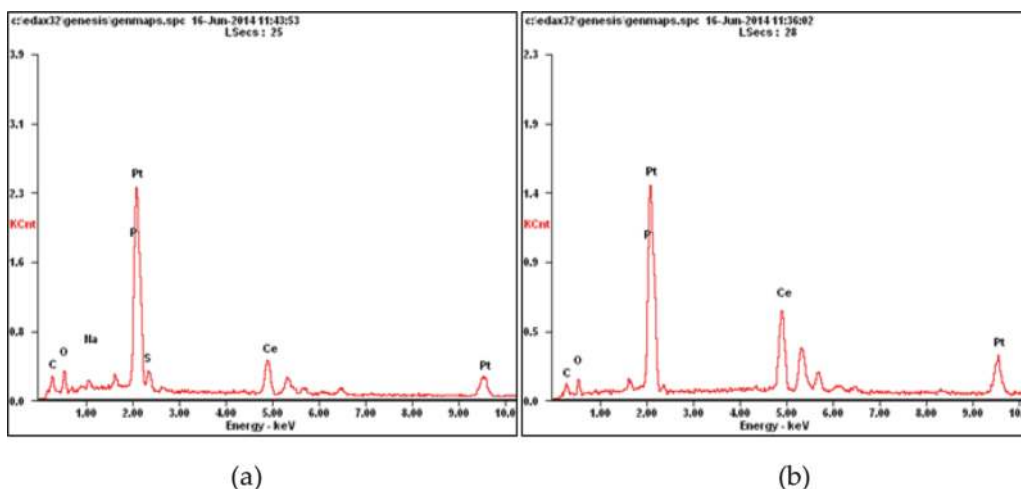


Figure 4. EDS spectra: (a) $\text{CePO}_4 @ \text{NaCe}(\text{SO}_4)_2(\text{H}_2\text{O})$ and (b) CePO_4 [15].

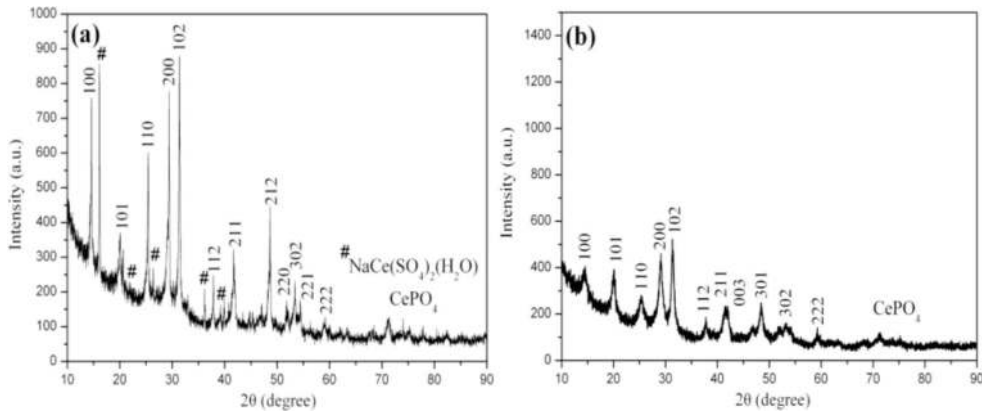


Figure 5. XRD patterns: (a) $CePO_4@NaCe(SO_4)_2(H_2O)$ and (b) $CePO_4$ [15].

Sample	P/Ce (molar ratio)	θ (deg)	β (deg)	D (nm)
$CePO_4$	2:1	15.67	0.504	15.61
$CePO_4@NaCe(SO_4)_2(H_2O)$	1:1	15.68	0.243	32.34

Table 1. Average crystallite size of cerium phosphates [15].

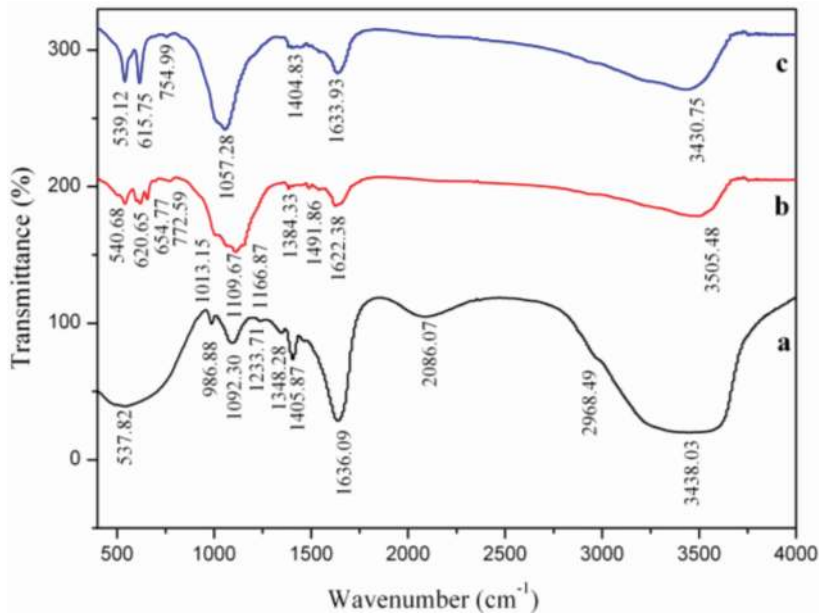


Figure 6. FTIR spectra: (a) *Bacillus subtilis*, (b) $CePO_4@NaCe(SO_4)_2(H_2O)$, and (c) $CePO_4$ [15].

Cerium phosphates and *Bacillus subtilis* were determined by FTIR spectra, as shown in **Figure 6**. According to literature reported, the peaks at 3438.03, 2968.49 and 1348.28, 1636.09, 1233.71, 1092.30, 1405.87, and 537.82 cm^{-1} corresponded to, respectively, OH, C-H, C=O or N-H, C-O, etc. (**Figure 3a**) [23]. Above results showed that these functional groups play important roles in the process of adsorption and reduction of Ce(IV) [23]. **Figure 6b** indicated the peak at 1013.15 cm^{-1} was attributed to the asymmetry stretching vibration of the PO_4^{3-} groups. The peaks

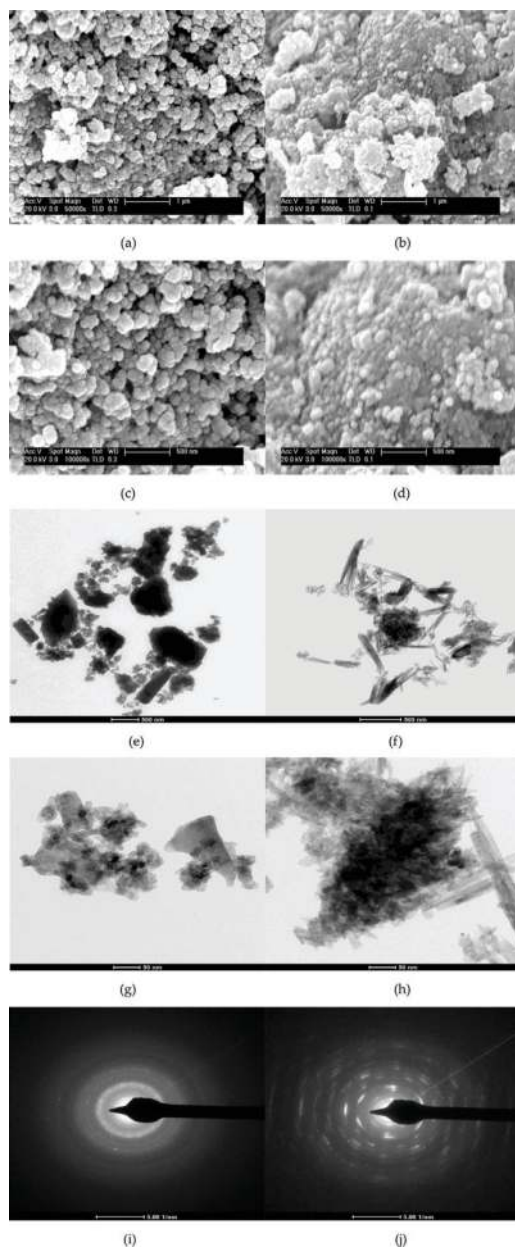


Figure 7. SEM images of $\text{CePO}_4@NaCe(\text{SO}_4)_2(\text{H}_2\text{O})$ (a, c) and CePO_4 (b, d), TEM images of $\text{CePO}_4@NaCe(\text{SO}_4)_2(\text{H}_2\text{O})$ (e, g) and CePO_4 (f, h), and ED images of $\text{CePO}_4@NaCe(\text{SO}_4)_2(\text{H}_2\text{O})$ (i) and CePO_4 (j) [15].

at 620.65 and 540.68 cm^{-1} were assigned to the O-P-O bending vibration [24]. The peaks at 1109.67 and 654.77 cm^{-1} corresponded to the stretching vibration of SO_4^{2-} group and the bending vibration of O-S-O, respectively. Weak transmission bands of PO_4 were at 1057.28 cm^{-1} and bending at 539.12 and 615.75 cm^{-1} , as shown in **Figure 6c**, in good agreement with the investigations on CePO_4 by Yang [24]. Other peaks in **Figure 6b** and **c** may be ascribed to the absorption vibration of N-H, C=O, COO^- , etc., according to the FTIR of *Bacillus subtilis*.

The morphology and crystalline nature of cerium phosphates were observed by SEM, TEM, and electron diffraction (ED) images, as shown in **Figure 7**. SEM images showed shape of $\text{CePO}_4@NaCe(\text{SO}_4)_2(\text{H}_2\text{O})$ and CePO_4 was nano-clusters and sphere-like with a narrow diameter distribution (**Figure 4a, b, c, and d**). TEM images further confirmed that a large number of nanoparticles were stacked

together and formed the big agglomerates. The size of $\text{CePO}_4@ \text{NaCe}(\text{SO}_4)_2(\text{H}_2\text{O})$ and CePO_4 was in the range of 20–50 nm and 5–25 nm, respectively. Nanosheets and nanorods in $\text{CePO}_4@ \text{NaCe}(\text{SO}_4)_2(\text{H}_2\text{O})$ and CePO_4 were observed, as shown in **Figure 7g** and **h**. ED patterns showed that $\text{CePO}_4@ \text{NaCe}(\text{SO}_4)_2(\text{H}_2\text{O})$ and CePO_4 nanomaterials were well crystallized, as shown **Figure 7i** and **j**.

5. Microbiological reduction-precipitation of nanostructured iron phosphates

FTIR spectrum of iron phosphates was observed in **Figure 8**. The broad peaks at $3000\text{--}3500\text{ cm}^{-1}$ and the strong peak at 1644.90 cm^{-1} were attributed to the O-H stretching vibration in water. The iron phosphates showed the peaks at 1056.82 and 553.89 cm^{-1} were stretching vibration of PO_4^{3-} groups [17–20, 21, 24–26]. O, P, and Fe elements were found in EDS spectrum, as shown in **Figure 9a**. Therefore, iron phosphates were composed by O, P, and Fe elements. XRD further confirmed iron phosphates could be readily indexed to the reported structures of $\text{Fe}_3(\text{PO}_4)_2 \cdot 8\text{H}_2\text{O}$ (JCPDS Card No.03–0070), and no peaks attributed to impurities (**Figure 9b**).

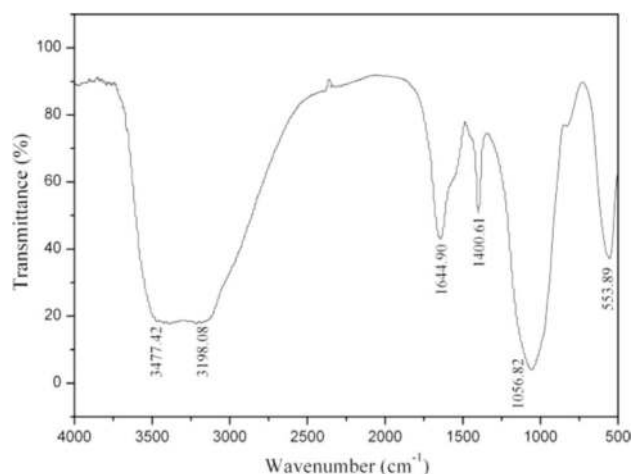


Figure 8.
FTIR spectrum of iron phosphates [16].

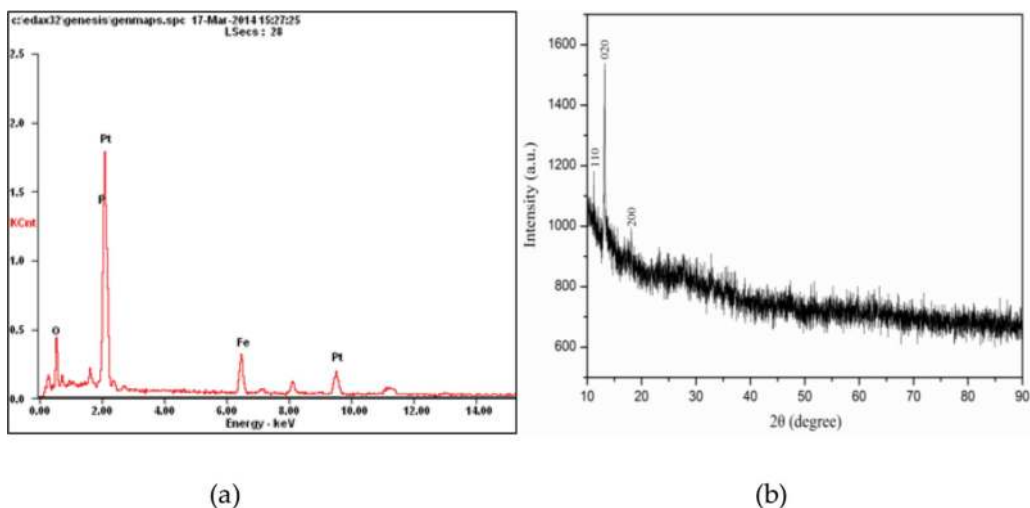


Figure 9.
EDS spectrum and XRD patterns of iron phosphates [16].

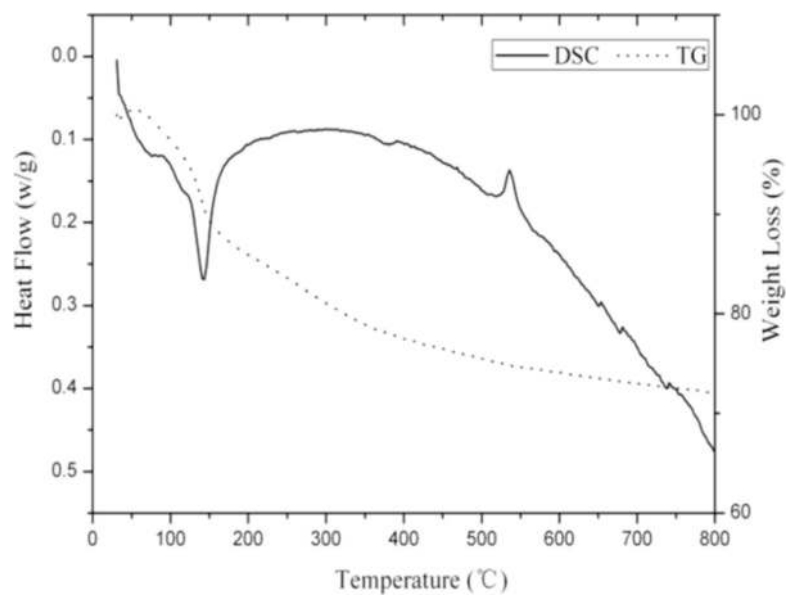


Figure 10.
TG-DSC curves of $\text{Fe}_3(\text{PO}_4)_2 \cdot 8\text{H}_2\text{O}$ [16].

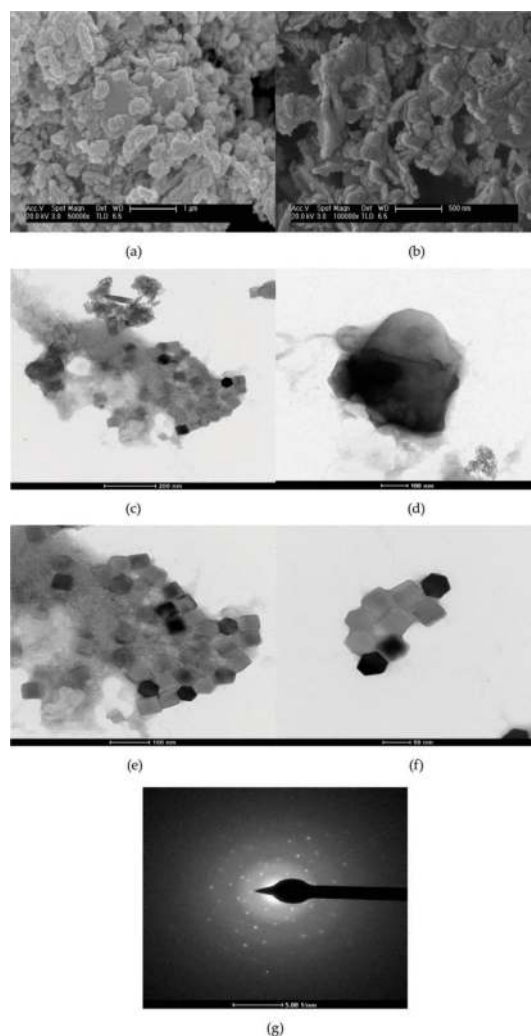


Figure 11.
SEM images (a, b), TEM images (c, d, e, f), and ED patterns (g) of $\text{Fe}_3(\text{PO}_4)_2 \cdot 8\text{H}_2\text{O}$ [16].

TG-DSC curves of iron phosphates were analyzed from room temperature to 800°C, as shown in **Figure 10**. The TG curve showed total weight loss was about 28.38%, which consisted with the theoretical value (28.69%). TG also confirmed chemical composition of iron phosphates was $\text{Fe}_3(\text{PO}_4)_2 \cdot 8\text{H}_2\text{O}$. Crystal water in $\text{Fe}_3(\text{PO}_4)_2 \cdot 8\text{H}_2\text{O}$ could be removed at temperature range of 61–250°C. DSC curve showed endothermic peaks at 142.1°C and 536.1°C were decomposition points of $\text{Fe}_3(\text{PO}_4)_2 \cdot 8\text{H}_2\text{O}$ and crystallization of $\text{Fe}_3(\text{PO}_4)_2$, respectively.

SEM, TEM, and ED images of $\text{Fe}_3(\text{PO}_4)_2 \cdot 8\text{H}_2\text{O}$ were observed in **Figure 11**. SEM images showed that the shape of $\text{Fe}_3(\text{PO}_4)_2 \cdot 8\text{H}_2\text{O}$ was honeycomb-like, as shown in **Figure 11a** and **b**. TEM images indicated that the morphology of $\text{Fe}_3(\text{PO}_4)_2 \cdot 8\text{H}_2\text{O}$ was quadrilateral, hexagonal, and irregular structure with size in the range of 20–200 nm (**Figure 11c, d, e, and f**). The average crystallite size was calculated through the Scherrer formula (1), which was 31.89 nm [13]. The ED patterns indicated $\text{Fe}_3(\text{PO}_4)_2 \cdot 8\text{H}_2\text{O}$ was polycrystalline in nature (**Figure 11g**).

6. Conclusions

1. *Bacillus subtilis* could hydrolyze organic phosphate monoester to form phosphate ions. Barium phosphate nanoparticles could well be prepared by the centrifuged solution of *Bacillus subtilis* and organic phosphate monoester reacting with barium ions under different pH. TEM images indicated that shape of barium phosphate particles was mainly irregular flakes. The average size of barium phosphates were 48.56, 36.60, 31.89, 33.27, and 34.79 nm when pH were 7, 8, 9, 10, and 11, respectively.
2. Nanostructures of CePO_4 and $\text{CePO}_4 @ \text{NaCe}(\text{SO}_4)_2(\text{H}_2\text{O})$ have been successfully synthesized through the mixture solution of *Bacillus subtilis* and organic phosphate monoester reacting with Ce(IV). The average crystalline size of CePO_4 and $\text{CePO}_4 @ \text{NaCe}(\text{SO}_4)_2(\text{H}_2\text{O})$ was 15.61 and 32.34 nm, respectively. TEM images indicated that shape of $\text{CePO}_4 @ \text{NaCe}(\text{SO}_4)_2(\text{H}_2\text{O})$ and CePO_4 was nanosheets and nanorods with nonuniform size, respectively.
3. FTIR spectrum, EDS, XRD, and TG-DSC confirmed the chemical composition of iron phosphates was $\text{Fe}_3(\text{PO}_4)_2 \cdot 8\text{H}_2\text{O}$. TEM images showed that the morphology of $\text{Fe}_3(\text{PO}_4)_2 \cdot 8\text{H}_2\text{O}$ powder was quadrilateral, hexagonal, and irregular in structure with the size of 31.89 nm.
4. The content of phosphate ions can be increased by adjusting the amount of substrate and pH in the mixture solution of *Bacillus subtilis* and organic phosphate monoester. At same time, the removal efficiency of heavy metal ions can well be increased in soil and water. The different phosphate nanomaterials can be prepared using centrifugation liquid or bacterial liquid.

Conflict of interest

The authors declare no conflict of interest.

Notes/thanks/other declarations

This work was supported by the National Nature Science Foundation of China (51702238) and the Opening Funds of Jiangsu Key Laboratory of Construction Materials (CM2018–02); the financial support is gratefully acknowledged.

Author details

Xiaoni Yu^{1,2} and Qiwei Zhan^{3*}

1 College of Civil Engineering and Architecture, Wenzhou University, Wenzhou, China

2 School of Environment, Tsinghua University, Beijing, China

3 School of Materials Science and Engineering, Anhui University of Technology, Maanshan, China

*Address all correspondence to: zhanqw@ahut.edu.cn

IntechOpen

© 2019 The Author(s). Licensee IntechOpen. This chapter is distributed under the terms of the Creative Commons Attribution License (<http://creativecommons.org/licenses/by/3.0>), which permits unrestricted use, distribution, and reproduction in any medium, provided the original work is properly cited. 

References

- [1] Pandey LK, Park J, Son DH, Kim W, Islam MS, Choi S, et al. Assessment of metal contamination in water and sediments from major rivers in South Korea from 2008 to 2015. *Science of the Total Environment*. 2019;**651**:323-333. DOI: 10.1016/j.scitotenv.2018.09.057
- [2] Gardener H, Bowen J, Callan SP. Lead and cadmium contamination in a large sample of United States infant formulas and baby foods. *Science of the Total Environment*. 2019;**651**:822-827. DOI: 10.1016/j.scitotenv.2018.09.026
- [3] Cheng H, Shen RL, Chen YY, Wan QJ, Shi TZ, Wang JJ, et al. Estimating heavy metal concentrations in suburban soils with reflectance spectroscopy. *Geoderma*. 2019;**336**:59-67. DOI: 10.1016/j.geoderma.2018.08.010
- [4] Shi TZ, Guo L, Chen YY, Wang WX, Shi Z, Li QQ, et al. Proximal and remote sensing techniques for mapping of soil contamination with heavy metals. *Applied Spectroscopy Reviews*. 2018, 2018;**3**:1-23. DOI: 10.1080/05704928.2018.1442346
- [5] Peng YT, Shen Y, Ge MY, Pan ZY, Chen WM, Gong B. Efficient extraction of heavy metals from collagens by sulfonated polystyrene nanospheres. *Food Chemistry*. 2019;**275**:377-384. DOI: 10.1016/j.foodchem.2018.09.111
- [6] Zhou WH, Liu FM, Yi SP, Chen YZ, Geng XY, Zheng CM. Simultaneous stabilization of Pb and improvement of soil strength using nZVI. *Science of the Total Environment*. 2019;**651**:877-884. DOI: 10.1016/j.scitotenv.2018.09.146
- [7] Shao JC, Yu XN, Zhou M, Cai XQ, Yu C. Nanoscale zero-valent iron decorated on bentonite/graphene oxide for copper ions removal from aqueous solution. *Materials*. 2018;**11**:945. DOI: 10.3390/ma11060945
- [8] Yu XN, Qian CX, He ZH, Sun LZ. Removal of heavy metal Ba (II) by phosphate-mineralization microbe under different standing time. *Fresenius Environmental Bulletin*. 2017;**26**:859-863
- [9] Qian CX, Zhan QW. Bioremediation of heavy metal ions by phosphate-mineralization bacteria and its mechanism. *Journal of the Chinese Chemical Society*. 2016;**63**:635-639. DOI: 10.1002/jccs.201600002
- [10] Qian CX, Xiaoniu Yu XN, Wang X. Potential uses and cementing mechanism of bio-carbonate cement and bio-phosphate cement. *AIP Advances*. 2018;**8**:095224. DOI: 10.1063/1.5040730
- [11] Li L, Qian CX, Cheng L, Wang RX. A laboratory investigation of microbe-inducing CdCO₃ precipitate treatment in Cd²⁺ contaminated soil. *Journal of Soils and Sediments*. 2010;**10**:248-254. DOI: 10.1007/s11368-009-0089-6
- [12] Yu XN, Qian CX, Wang X. Biosynthesis of magnesium phosphates and its thermal property. *Science of Advanced Materials*. 2015;**7**:1730-1733. DOI: 10.1166/sam.2015.2392
- [13] Wang X, Qian CX, Yu XN. Synthesis of nano-hydroxyapatite via microbial method and its characterization. *Applied Biochemistry and Biotechnology*. 2014;**173**:1003-1010. DOI: 10.1007/s12010-014-0911-5
- [14] Yu XN, Qian CX, Wang X. Bio-inspired synthesis of barium phosphates nanoparticles and its characterization. *Digest Journal of Nanomaterials and Biostructures*. 2015;**10**:199-205
- [15] Yu XN, Qian CX. Biological reduction-deposition and luminescent properties of nanostructured CePO₄@

- NaCe(SO₄)₂(H₂O) and CePO₄.
Materials Chemistry and Physics.
2016;**171**:346-351. DOI: 10.1016/j.
matchemphys.2016.01.026
- [16] Yu X, Wang X, Qian C. Micro-
biological mineralization: Bacillus-
induced Vivianite Fe₃(PO₄)₂·8H₂O
precipitation. Digest Journal of
Nanomaterials and Biostructures.
2014;**9**:1373-1378
- [17] Nallamuthu D, Selvarajan P, Freeda
TH. Studies on various properties of
pure and Li-doped barium hydrogen
phosphate (BHP) single crystals.
Physica B: Condensed Matter.
2010;**405**:4908-4913. DOI: 10.1016/j.
physb.2010.09.030
- [18] Arora SK, Trivedi TR, Oza AT,
Patel VA. IR spectroscopy of barium
hydrogen phosphate. Acta Materialia.
2001;**49**:2103-2107. DOI: 10.1016/
s1359-6454(01)00024-6
- [19] Höpfe HA, Daub M, Oeckler O.
Synthesis, crystal structure, infrared
spectrum and thermal behaviour of
α-BaHPO₄. Solid State Sciences.
2009;**11**:1484-1488. DOI: 10.1016/j.
solidstatesciences.2009.05.007
- [20] Hebbar KC, Dharmaprakash SM,
Rao PM. Growth of barium hydrogen
phosphate crystals. Journal of Materials
Science Letters. 1991;**10**:1430-1432.
DOI: 10.1007/BF00724398
- [21] Dinamani M, Vishnu Kamath P.
Electrochemical synthesis of metal
phosphates by cathodic reduction.
Materials Research Bulletin.
2001;**36**:2043-2050. DOI: 10.1016/
S0025-5408(01)00682-1
- [22] Wang F, Xu GY, Zhang ZQ. The
effect of pH on morphological control
of barium hydrogen phosphate crystal
by a double-hydrophilic copolymer.
Materials Letters. 2005;**59**:808-812.
DOI: 10.1016/j.matlet.2004.11.026
- [23] Ji Y, Gao H, Sun J, Cai F.
Experimental probation on the binding
kinetics and thermodynamics of
Au(III) onto Bacillus subtilis. Chemical
Engineering Journal. 2011;**172**:122-128.
DOI: 10.1016/j.cej.2011.05.077
- [24] Yang M, You H, Zheng Y, Liu K, Jia
G, Song Y, et al. Hydrothermal synthesis
and luminescent properties of novel
ordered sphere CePO₄ hierarchical
architectures. Inorganic Chemistry.
2009;**48**:11559-11565. DOI: 10.1021/
ic901829v
- [25] Frost RL, Weier ML. Raman
spectroscopic study of vivianites of
different origins. Neues Jahrbuch
fuer Mineralogie-Monatshefte.
2004;(10):445-463. DOI:
10.1127/0028-3649/2004/2004-0445
- [26] Walpersdorf E, Koch CB, Heiberg
L, O'Connell DW, Kjaergaard C, Hansen
HCB. Does vivianite control phosphate
solubility in anoxic meadow soils?
Geoderma. 2013;**193-194**:189-199. DOI:
10.1016/j.geoderma.2012.10.003